Thin–Walled Structures 228 (2026) 115068

Contents lists available at ScienceDirect

Thin-Walled Structures

journal homepage: www.elsevier.com/locate/tws

Full Length Article

Superelastic SMA omega dampers for seismic resilience

Shuling Hu [a,b], Jinmeng Zang [a], Tong Guo [a], Zhi-Peng Chen [a,*], Theodoros L. Karavasilis [b], M. Shahria Alam [c], Vasileios C. Kamperidis [d]

[a] School of Civil Engineering, Southeast University, Nanjing, China
[b] Department of Civil Engineering, University of Patras, Patras 26504, Greece
[c] School of Engineering, The University of British Columbia, Kelowna, BC V1V 1V7, Canada
[d] Department of Civil Engineering, Neapolis University Pafos, Paphos 8042, Cyprus

ARTICLE INFO

Keywords:
Shape memory alloy
Self-centering
Residual deformation
Tests
Numerical study

ABSTRACT

This paper aims to develop a novel shape memory alloy (SMA) omega damper (denoted as SMA-Ω damper) as a new self-centering component for developing seismic resilient engineering structures. The mechanical behavior and deformation mechanism of the SMA-Ω damper were presented firstly. Experimental studies were subsequently conducted to investigate its hysteretic behavior and failure mode under cyclic loadings. Test results confirmed that the proposed SMA-Ω dampers could achieve reliable self-centering performance with negligible residual deformations under cyclic loadings. Parametric numerical studies were further carried out to understand the strain and stress development in SMA-Ω dampers under cyclic loading and to investigate the influence of design parameters. Parametric analyses revealed that the geometric parameters t, R, r, and d_1 governed stiffness, strength, and strain distribution. Larger thickness (t), smaller radii (R, r), and shorter transition lengths (d_1) increased stiffness, strength, and energy-dissipation capacity but might induce stress concentration and reduce deformation capacity. Based on the test and numerical results, the design recommendations of SMA-Ω dampers were finally proposed.

1. Introduction

Earthquakes are one of the most severe disasters for modern structures and infrastructures [1,2]. The plastic design method is widely adopted in modern seismic design guidelines (e.g., Eurocode 8 [3], GB 50011-2010 [4], and ASCE 7–16 [5]). Plastic behavior with sufficient ductility is encouraged to achieve reliable energy-dissipation capacities against structural collapse under strong earthquakes [6–8]. Nevertheless, plastic behavior inevitably introduces considerable residual deformations [9–11]. Fahnestock et al. [12] found that the residual deformation of traditional buckling-restrained braced frames (BRBFs) after maximum considered earthquakes (MCEs) is up to 1.2%. Erochko et al. [13] pointed out that residual drifts of BRBFs and moment-resisting frames designed based on existing design codes are, on average, between 2.0% and 4.0%. These significant residual displacements pose a serious threat to the safety of structures during aftershocks and severely hinder the post-earthquake repair and functional recovery of the structures. According to FEMA P−58 [14], major structural realignment is required to restore the margin of safety for lateral stability of the structure with a residual story drift ratio over 1.0% and this realignment may not be economically and practically feasible. After the 2011 Christchurch earthquake, a substantial number of non-collapse structures underwent demolition due to severe residual deformations, leading to extensive economic loss [15]. The residual deformation becomes an essential index for designing [16–18] and evaluating [19–21] engineering structures, and reducing post-earthquake residual displacements is a crucial task for the development of the next generation of seismic-resistant engineering structures and reducing the life-cycle costs induced by earthquakes [22,23].

Shape memory alloys (SMAs) constitute a distinctive category of metals with the ability to recover significant strains either through heating (shape memory effect) or spontaneously (superelastic effect), contingent on their thermal-mechanical condition [24,25]. Superelastic Ni-Ti SMA is the most popular class, showing stable superelastic behavior at room temperature. The typical stress-strain responses of superelastic Ni-Ti SMA are plotted in Fig. 1, which is realized by the solid-to-solid transformation between the austenite and martensite phases. The austenite finish temperature can be set below ambient

* Corresponding author.
E-mail address: zpchen_edu@seu.edu.cn (Z.-P. Chen).

https://doi.org/10.1016/j.tws.2026.115068
Received 11 February 2026; Received in revised form 15 April 2026; Accepted 2 May 2026
Available online 5 May 2026
0263-8231/© 2026 Elsevier Ltd. All rights are reserved, including those for text and data mining, AI training, and similar technologies.

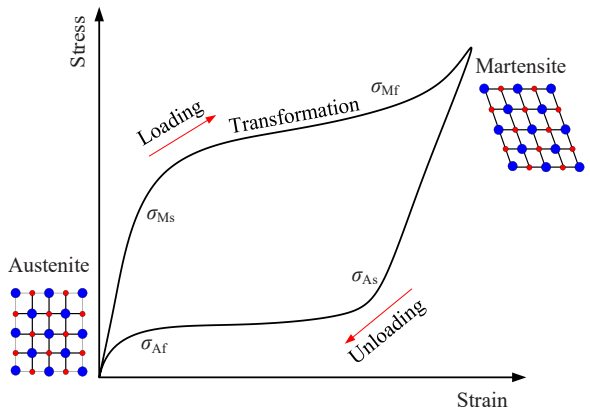

Fig. 1. Superelastic hysteretic behavior of Ni-Ti SMA.

temperature using modern mature manufacturing technology. Without loading, the superelastic Ni-Ti SMA can remain in the austenite phase. Loading will activate the austenite-to-martensite transformation, and unloading will activate the martensite-to-austenite transformation, resulting in flag-shaped hysteretic behavior with restrained residual deformation and moderate hysteretic energy dissipation. The recoverable strain of superelastic Ni-Ti SMA is up to 8% at room temperature [26]. This unique behavior makes superelastic Ni-Ti SMA a promising solution to reduce structural residual deformations under earthquakes. Note that superelastic Ni-Ti SMA is simply referred to using SMA in the following parts of this paper.

Table 1 summarizes the SMA components developed for seismic applications in previous publications. The existing SMA components can be divided into three types [73], including axial, bending, and hoop. The axial SMA components include wires, cables, bars, plates, buckling-restrained bars, and buckling-restrained plates. They utilize the axial tension or compression behavior of SMA material. The bending SMA components include angles and U-shaped plates. They utilize the tension and compression behavior of SMA material in the same section through the bending deformation mechanism. The hoop SMA components include disc rings, outer friction springs, and rings. They utilize the tension or compression behavior of SMA material through radial deformation. These components were originally made of steel. The use of SMA materials enables these components to possess both self-centering and energy-dissipation capabilities simultaneously. Each of these elements possesses distinct advantages and drawbacks in mechanical performance, manufacturing processes, connectivity, etc., rendering them suitable for diverse application scenarios. They have found widespread application in the development of self-centering braces, beam-to-column connections, column bases, bridge columns, link beams, isolators, and related components. Compared with alternative types, bending-type SMA components exhibit a unique capability to alleviate cumulative residual deformations and mitigate loading capacity deterioration under cyclic loading, leveraging the bending deformation mechanism. Additionally, the utilization of the tension-compression behavior of SMA materials enables bending-type SMA components to circumvent the loss of loading capacity observed in tension SMA components due to cumulative residual deformations.

Although various SMA dampers exist (as shown in Table 1), current components still fall short in balancing high deformation capacity with low stress concentration. Therefore, this study aims to address the brittle fracture problem of SMA dampers under complex stress states by proposing a novel Omega configuration (denoted as SMA-Ω damper). This study focuses on (1) theoretically proposing the geometric configuration

Table 1
Summary of existing SMA components.

Type	Components	Mechanical behavior	Advantages	Disadvantages	Application
Axial	Wire [24,27]	Tension	Mature manufacturer, good quantity	Low loading capacity, difficult anchoring, cumulative residual deformation, loading capacity deterioration	Brace[28–30], isolator[31], composite beam[32]
	Cable [33–35]	Tension	High loading capacity, good quantity, non-abrupt fracture	Difficult anchoring, cumulative residual deformation, loading capacity deterioration	Brace[36,37], isolator[38,39], reinforced concrete[40]
	Bar[41,42]	Tension	High loading capacity, good quality	Difficult manufacture of connection, abrupt fracture, cumulative residual deformation, loading capacity deterioration	Brace[43], beam-to-column connection[44,45], column[46,47], reinforced concrete beam[48], isolator [49], wall[50]
	Plate[51,52]	Tension	High loading capacity, good quantity, easy connection	Cumulative residual deformation, loading capacity deterioration	Beam-to-column connection[53], self-centering damper[54]
	Buckling-restrained bar [55,56]	Tension-compression	High loading capacity, good quantity, high utilization of material	Additional buckling restrained device, difficult manufacture of connection, abrupt fracture, cumulative residual deformation, loading capacity deterioration	Knee brace[57], self-centering damper [58]
	Buckling-restrained plate [59]	Tension-compression	High loading capacity, good quantity, high utilization of material, easy connection	Additional buckling restrained device, cumulative residual deformation, loading capacity deterioration	Beam-to-column connection[51]
Bending	Angle[60,61]	Tension-compression	easy connection, restrained cumulative residual deformation, and loading capacity deterioration	High cost of manufacture, premature fracture	Eccentrically braced frame[62], beam-to-column connection[61]
	U-shaped plate [63,64]	Tension-compression	easy connection, restrained cumulative residual deformation and loading capacity deterioration, Flexible deformability	High cost of manufacture, premature fracture	Brace, isolator[65]
Hoop	Disc spring[66, 67]	Tension-compression	Flexible deformability	High cost of manufacture, small loading capacity, cumulative residual deformation, loading capacity deterioration	beam-to-column connection[67]
	Outer friction spring[68]	Tension	High loading capacity, excellent energy dissipation	High cost of manufacture, cumulative residual deformation, loading capacity deterioration	Brace[69], beam-to-column connection[70]
	Ring[71,72]	Tension-compression	High loading capacity	Cumulative residual deformation, the requirement of special connection	Brace[71]

Note: A common problem with the above components is that when the SMA material enters the late stage of phase transformation, the sudden increase in stiffness prevents the full development of plastic hinges, leading to brittle fracture at geometric discontinuities.

and deformation mechanism of the SMA-Ω damper; (2) experimentally validating its self-centering capability and failure mode through quasi-static testing; and (3) numerically revealing the influence of geometric parameters on performance through parametric analysis. The remainder of the paper is organized as follows: Section 2 will preliminarily introduce the working mechanism and mechanical behavior of SMA-Ω dampers; Section 3 will present the validation tests for the proposed SMA-Ω damper under cyclic loadings; Section 4 will conduct parametric numerical simulations to understand the strain and stress development in SMA-Ω dampers under cyclic loading and investigate the influence of design parameters; Section 5 will summarize the remarkable findings; and Section 6 presents the limitations and future work.

2. Working mechanism and mechanical behavior of SMA-Ω damper

Fig. 2 sketches the proposed SMA-Ω damper. The SMA-Ω damper is developed based on the steel pi damper proposed by Koetaka et al. [74]. As illustrated in Figs. 2(a) and 2(b), the pi damper and Ω damper all consist of a U-shaped segment and two flat segments. The U-shaped segment consists of a semicircular plate and two vertical plates. The height of the pi and Ω dampers can be easily controlled by adjusting the length of the vertical plates. The pi and the Ω dampers differ in two aspects. First, in the pi damper, the flat segment is thicker than the U-shaped segment, whereas in the Ω damper, the flat and U-shaped segments have equal thickness. Second, in the pi damper, the flat and U-shaped segments are connected by a single-sided circular transition, while in the Ω damper, they are joined by a quarter-circle plate. This Ω damper configuration minimizes stress concentration at the section transition and thereby improves structural ductility, as validated through comparative tests in Section 3. The proposed SMA-Ω damper can be easily connected to adjacent structural members using bolts, enabling rapid construction and convenient post-earthquake replacement if necessary.

As shown in Fig. 2(c), the SMA-Ω damper can transfer the axial tension or compression deformation to the bending of the U-shaped segment and the quarter-circle plate. The flexible deformation will activate the SMA material to provide self-centering and energy-absorbing capacities. The strength of the SMA-Ω damper can be flexibly designed by adjusting the thickness, width, and height of the U-shaped segment, the semicircular radius, and the quarter-circular radius.

The mechanical model of the SMA-Ω damper can be simplified as shown in Fig. 3, where the U-shaped segment, junctions between the U-shaped and flat segments, and the non-connected flat segments are modeled using beam elements, and the connected flat segments are modeled using rigid elements. The nonlinear behavior of the SMA-Ω

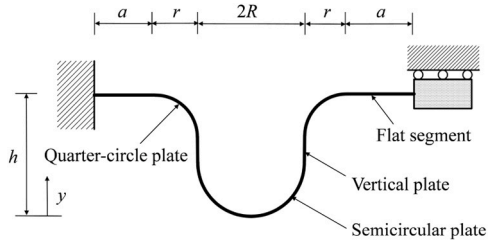

Fig. 3. Analytical model of SMA-Ω damper.

damper is characterized by the SMA material properties and the geometries in Fig. 2(b), including b, t, r, R, d_1, and d_2. In this study, the stiffness of the SMA-Ω dampers is evaluated using the elastic-center method and the force method. A coordinate system is established as shown in Fig. 4. The elastic center of the SMA-Ω damper can be computed by the following equation:

$$\bar{y} = \frac{\int \frac{y}{EI} ds}{\int \frac{1}{EI} ds} \tag{1}$$

in which EI denotes the flexural rigidity of the SMA-Ω damper cross-section. The integral in the denominator of Eq. (1) can be evaluated using Eq. (2):

$$\int \frac{1}{EI} ds = \frac{\frac{\pi R}{2} + \frac{\pi r}{2} + d_1 + d_2}{EI} \tag{2}$$

The numerator integral in Eq. (1) can be decomposed into four segments. As shown in Fig. 4, the integral for the upper quarter-circular arc can be calculated as:

$$\int_{s_1}^{s_2} \frac{y}{EI} ds = \int_0^{\pi/2} \frac{R(1 - \cos\theta) \cdot R \cdot d\theta}{EI} = \frac{\left(\frac{\pi}{2} - 1\right) R^2}{EI} \tag{3}$$

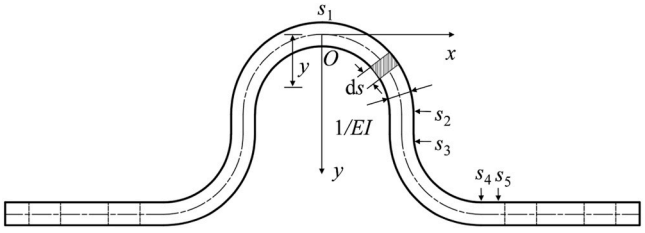

Fig. 4. The coordinate system for the SMA-Ω damper.

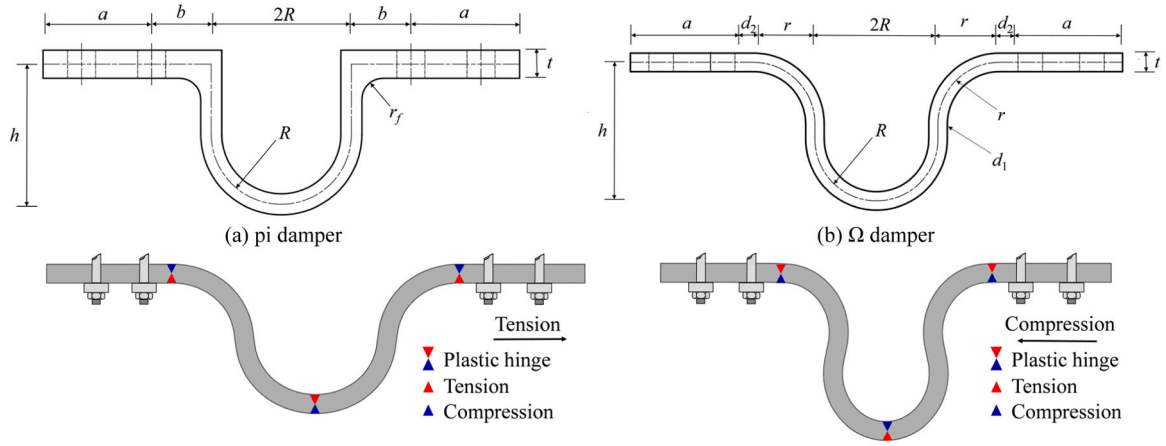

(c) deformation mechanism of the Ω damper

Fig. 2. Illustration of the considered dampers.

The integral for the connecting plate between the upper and lower quarter-circular arcs:

$$\int_{s_2}^{s_3}\frac{y}{EI}ds=\int_{R}^{R+d_1}\frac{y}{EI}dy=\frac{(R+d_1)^2-R^2}{2EI} \tag{4}$$

The integral for the lower circular arc:

$$\int_{s_3}^{s_4}\frac{y}{EI}ds=\int_{0}^{\pi/2}\frac{(R+d_1+r\cdot\sin\theta)\cdot rd\theta}{EI}=\frac{\left(R+d_1\right)r\frac{\pi}{2}+r^2}{EI} \tag{5}$$

The integral for the horizontal segment:

$$\int_{s_4}^{s_5}\frac{y}{EI}ds=\frac{(R+r+d_1)d_2}{EI} \tag{6}$$

Accordingly, the elastic center of the SMA-Ω damper can be computed by:

$$\overline{y}=\frac{\left[(\pi/2-1)R^2+Rd_1+\frac{1}{2}{d_1}^2+\frac{\pi}{2}\left(R+d_1\right)r+r^2+\left(R+r+d_1\right)d_2\right]}{\pi R/2+\pi r/2+d_1+d_2} \tag{7}$$

It should be noted that, unless otherwise stated, the line integrals are taken along the centroidal (mid-line) of each segment. In this study, only the flexural deformation of the cross-section is considered, and the axial and shear deformations are neglected. According to the force method, the horizontal displacement produced by a unit force can be evaluated as:

$$\delta_{11}=\int\frac{(y-\overline{y})^2}{EI}ds=\int\frac{y^2-2y\overline{y}+\overline{y}^2}{EI}ds=\delta_{111}+\delta_{112}+\delta_{113} \tag{8}$$

$$\delta_{111}=\frac{1}{EI}\int y^2ds=\frac{1}{EI}\int_{s_1}^{s_2}y^2ds+\frac{1}{EI}\int_{s_2}^{s_3}y^2ds+\frac{1}{EI}\int_{s_3}^{s_4}y^2ds+\frac{1}{EI}\int_{s_4}^{s_5}y^2ds \tag{9}$$

$$\begin{aligned}\delta_{112}&=-\frac{2\overline{y}}{EI}\int yds\\&=-\frac{2\overline{y}}{EI}\left[(\pi/2-1)R^2+Rd_1+\frac{1}{2}{d_1}^2+\frac{\pi}{2}\left(R+d_1\right)r+r^2+\left(R+r+d_1\right)d_2\right]\end{aligned} \tag{10}$$

$$\delta_{113}=\frac{\overline{y}^2}{EI}\int ds=\frac{\overline{y}^2}{EI}\left(\frac{\pi R}{2}+\frac{\pi r}{2}+d_1+d_2\right) \tag{11}$$

The numerator integral in Eq. (9) can be decomposed into four segments. As shown in Fig. 4, the integral for the upper quarter-circular arc can be calculated as:

$$\frac{1}{EI}\int_{s_1}^{s_2}y^2ds=\frac{R^3}{EI}\int_{0}^{\pi/2}(1-\cos\theta)^2d\theta=\frac{R^3}{EI}\left(\frac{3}{4}\pi-2\right) \tag{12}$$

The integral for the connecting plate between the upper and lower quarter-circular arcs:

$$\frac{1}{EI}\int_{s_2}^{s_3}y^2ds=\int_{R}^{R+d_1}\frac{y^2}{EI}dy=\frac{(R+d_1)^3-R^3}{3EI} \tag{13}$$

The integral for the lower circular arc:

$$\begin{aligned}\frac{1}{EI}\int_{s_3}^{s_4}y^2ds&=\int_{0}^{\pi/2}\frac{(R+d_1+r\cdot\sin\theta)^2\cdot r}{EI}d\theta\\&=\frac{\frac{\pi}{2}(R+d_1)^2r+2\left(R+d_1\right)r^2+\frac{\pi}{4}r^3}{EI}\end{aligned} \tag{14}$$

The integral for the horizontal segment:

$$\frac{1}{EI}\int_{s_4}^{s_5}y^2ds=\frac{(R+r+d_1)^2d_2}{EI} \tag{15}$$

Accordingly, δ_{11} can be computed by:

$$\begin{aligned}\delta_{11}=&\frac{R^3}{EI}\left(\frac{3}{4}\pi-2\right)+\frac{\frac{\pi}{2}(R+d_1)^2r+2\left(R+d_1\right)r^2+\frac{\pi}{4}r^3}{EI}+\frac{(R+d_1)^3-R^3}{3EI}+\frac{(R+r+d_1)^2d_2}{EI}\\&+\frac{\overline{y}^2}{EI}\left(\frac{\pi R}{2}+\frac{\pi r}{2}+d_1+d_2\right)-\frac{2\overline{y}}{EI}\left[(\pi/2-1)R^2+Rd_1+\frac{1}{2}{d_1}^2+\frac{\pi}{2}\left(R+d_1\right)r+r^2+\left(R+r+d_1\right)d_2\right]\end{aligned} \tag{16}$$

The initial stiffness of the SMA-Ω damper can be obtained as:

$$k=\frac{1}{\delta_{11}} \tag{17}$$

When the loading strength is larger enough to make the maximum stress greater than σ_{Ms} shown in Fig. 1, SMA materials start to transform from the austenite phase to the martensite phase, leading to the yield-like nonlinear behavior. It is worth noting that no yielding or plastic behavior occurs in SMA in this stage. For convenient reference, the strength associated with the austenite-to-martensite transformation is referred to using the yield strength of the SMA-Ω damper. As shown in Fig. 5, three plastic hinges are expected to occur in SMA-Ω dampers, including one at the midpoint and two at the end of the lower quarter-circular arc plate. In Fig. 5, F_y is the yielding strength, δ_y is the yielding deformation, θ_y is the yielding rotation, and M_y is the yielding moment. Eq. (18) can be obtained based on the conservation of energy:

$$F_y\delta_y=M_y\left(4\theta_y\right) \tag{18}$$

$$M_y=\frac{bt^2\sigma_{Ms}}{4} \tag{19}$$

Based on the geometrical relation, δ_y can be calculated as:

$$\delta_y=2\left[h_y\sin\theta_y+(R+r)\cos\theta_y-(R+r)\right] \tag{20}$$

By assuming small deformations, $\sin\theta_y$ can be taken as θ_y, and $\cos\theta_y$ can be taken as 1. Accordingly, Eq. (20) can be rewritten as:

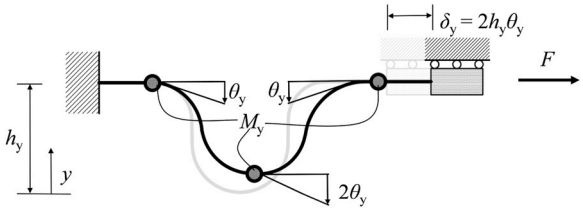

Fig. 5. Yielding mechanism of the SMA-Ω damper.

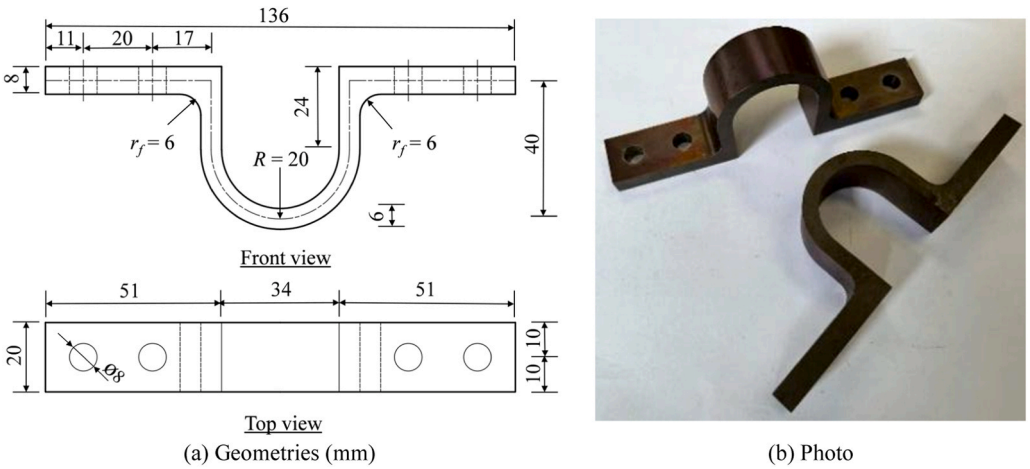

(a) Geometries (mm) (b) Photo

Fig. 6. Specimen of SMA-pi damper.

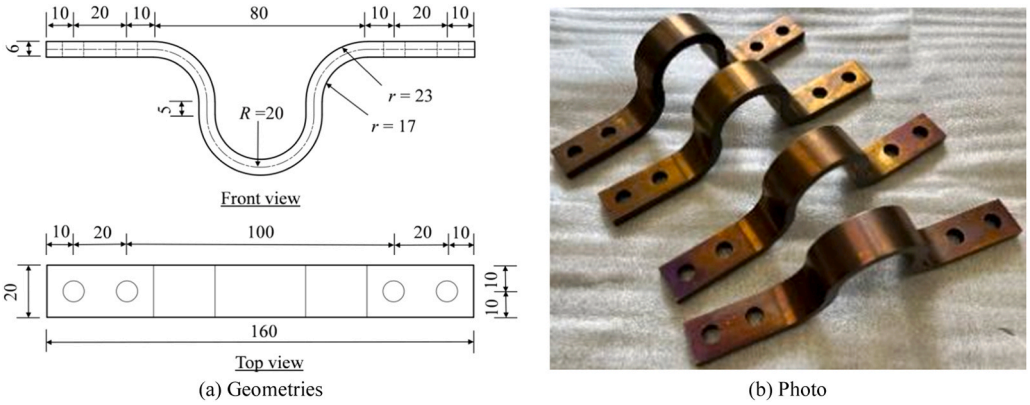

(a) Geometries (b) Photo

Fig. 7. Specimen of SMA-Ω damper.

$$\delta_y = 2h_y\theta_y = 2(r + d_1 + R)\theta_y \tag{21}$$

By substituting Eq. (21) and Eq. (19) into Eq. (18), a closed-form expression for F_y can be obtained:

$$F_y = \frac{bt^2\sigma_{Ms}}{2(r + d_1 + R)} \tag{22}$$

The von Mises yield criterion is adopted to consider the biaxial stress state with $2/\sqrt{3}$ times the uniaxial yield stress:

$$F_y = \frac{bt^2\sigma_{Ms}}{\sqrt{3}(r + d_1 + R)} \tag{23}$$

3. Validation tests

3.1. Design and manufacture of SMA-Ω damper specimens

SMA-Ω and SMA-pi damper specimens were designed for comparative purposes. Figs. 6 and 7 show their geometries and photographs. The SMA-Ω and SMA-pi damper specimens have the same width (i.e., 20 mm) and thickness of the U-shaped segment (i.e., 6 mm). The thickness of the SMA-pi damper's flat segment is 8 mm, which is higher than that of the U-shaped segment (i.e., 6 mm) to ensure that the nonlinear behavior only develops in the U-shaped segment. The centerline radius of the semicircular plates in the U-shaped segments of both dampers is 20 mm. In the SMA-pi damper, the radius of the circular transition between the flat and U-shaped segments is 6 mm. In the SMA-Ω damper, the centerline radius of the quarter-circle plates is 20 mm. Two bolt holes with a diameter of 8 mm were arranged in each flat segment to assemble the SMA-pi and SMA-Ω dampers to the loading plate through steel bolts. The SMA-pi and SMA-Ω damper specimens were manufactured by cutting the superelastic SMA plate with a thickness of 20 mm by wire electrical discharge machining technology. The polishing process was included in the manufacturing of specimens to eliminate surface defects generated during cutting. All manufactured SMA-Ω damper specimens underwent heat treatment by being subjected to 510 ℃ for a duration of 12 min in an electrical furnace, followed by rapid water quenching. As per the supplier-provided information, the superelastic SMA material possesses an austenite finish temperature (A_f) proximate to 0 – 5 °C. This characteristic ensures the superelastic behavior of the manufactured SMA-Ω damper specimens at room temperature. The price of the manufactured SMA-Ω damper is about 2000 USD/kg, which is useful for investigating the life-cycle benefits of structures adopting the proposed SMA-Ω dampers.

3.2. Experimental arrangement

The experimental setup was arranged to simulate the relative axial deformation of structural members connected using the proposed SMA-Ω dampers. As shown in Fig. 8(a), two SMA-Ω or SMA-pi dampers were symmetrically connected to the stiff steel plates through bolts. The stiff steel plates have a thickness of 20 mm and are made of Q345 steel with a nominal yield strength of 345 MPa. The loading protocol adopted in this study was developed with reference to FEMA 461 [75]. As shown in Fig. 8(b), displacement-controlled cyclic loading with stepwise increasing displacement amplitudes was used, and two cycles were

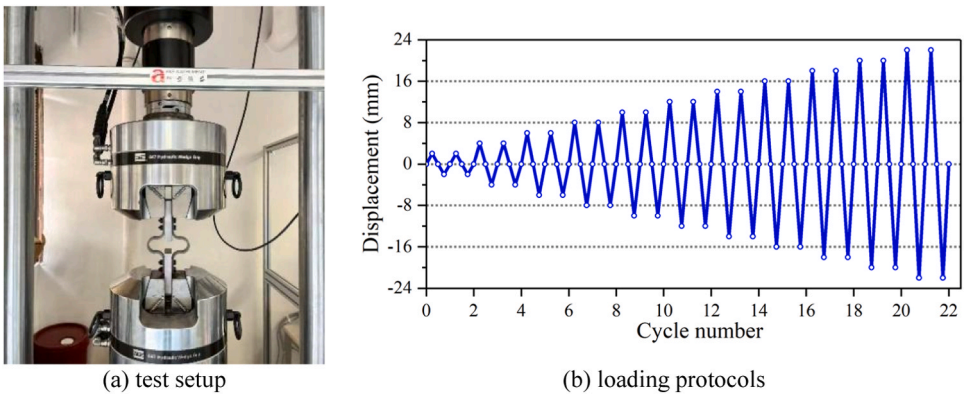

Fig. 8. Test setup and loading protocols.

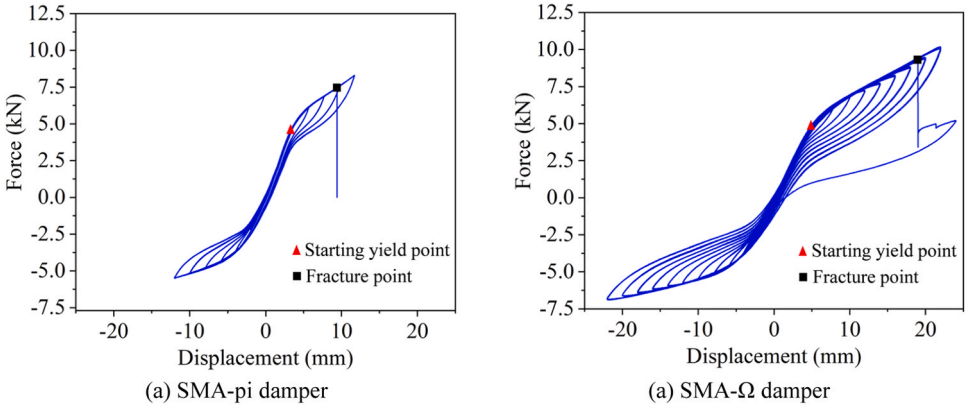

Fig. 9. Test Results.

applied at each displacement amplitude to capture the cyclic response and possible degradation characteristics of the damper while maintaining a reasonable test duration. The cyclic tests were conducted under a consistent loading rate of 0.1 mm/s at a room temperature of about 25 ℃. The internal data acquisition system of the MTS machine was utilized for measuring both forces and displacements of the tested specimens.

3.3. Test results

3.3.1. Hysteretic behavior

Fig. 9 shows the test results of the SMA-pi and Ω damper specimens, where the force was provided by two dampers. As shown in Fig. 9(a), compared to the traditional steel pi damper [74], which exhibits full and stable hysteresis loops, the SMA-pi damper shows a typical flag-shaped hysteretic response, characterized by reduced energy dissipation but significantly smaller residual deformations. The deformation capacity of the SMA-pi damper is also lower, with a maximum ductility of 3.12. This behavior stems from the unique material characteristics of SMA. During the austenite-to-martensite phase transformation, SMA exhibits a stress plateau similar to the yielding stage of steel. Once the austenite is fully transformed into martensite, however, the material undergoes an abrupt increase in stiffness. This sudden post-transformation hardening prevents the formation and spread of plastic hinges in SMA components, making them more sensitive to stress concentrations than their steel counterparts. As shown in Fig. 10(a), the SMA-pi damper eventually

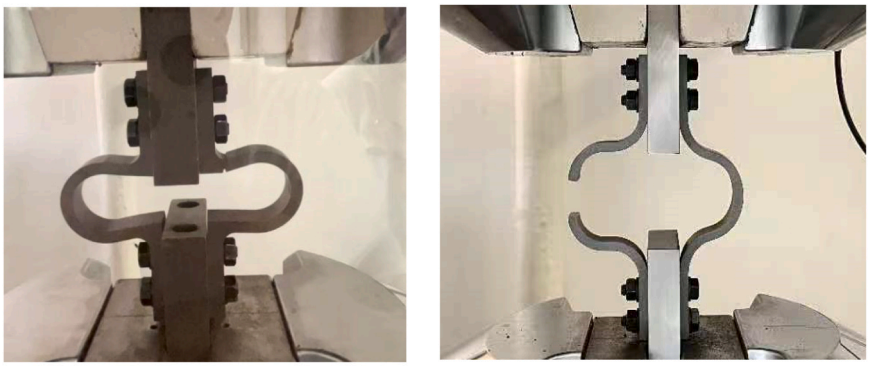

Fig. 10. Fracture of SMA-pi and Ω damper.

fractured at the circular transition between the flat and U-shaped segments, where the stress concentration is the most severe. In contrast, the SMA-Ω damper connects the flat and U-shaped segments through quarter-circle plates, effectively relieving stress concentration and achieving a markedly improved deformation capacity, as shown in Fig. 9 (b). The SMA-Ω damper exhibits a ductility ratio of 3.90, which is 1.25 times that of the SMA-pi damper. As shown in Fig. 10(b), the Ω damper ultimately fractured at the top of the U-shaped segment, representing the desired failure mode.

Compared with SMA axial members (e.g., SMA bars or wires), the SMA-Ω damper demonstrates a more pronounced hardening behavior after entering the nonlinear regime (analogous to "post-yield" behavior). This difference arises because axial SMA members experience relatively uniform stress and strain along the cross-section, whereas the bending deformation of the Ω damper leads to highly non-uniform strain distribution. Consequently, the outer "fibers" of the cross-section undergo the forward austenite-to-martensite transformation earlier than the inner "fibers". This unsynchronized phase transformation produces a more significant "post-yield" hardening in the hysteretic response of the Ω damper. Moreover, the SMA-Ω damper also exhibits asymmetric behavior in tension and compression. This phenomenon results from the stress/strain states and deformation modes in the two loading directions. As illustrated in Fig. 11, the height of the SMA-Ω damper decreases under tension and increases under compression. Section 4 will further investigate the stress and strain distribution patterns of the SMA-Ω damper under both tension and compression through refined finite element analyses.

3.3.2. Loading capacity

Fig. 12(a) shows the average yield strength of the SMA-Ω damper under different loading displacements. According to the MIIT definition [76], the yield point is identified as the intersection between the extrapolated linear segments of the austenite phase and the austenite-to-martensite transformation phase. It can be observed that the yield strength of the SMA-Ω damper exhibits only minor variation under different loading displacements, with the maximum difference being approximately 0.351 kN. Fig. 12(b) presents the peak strength of the SMA-Ω damper at various loading cycles. Owing to the distinct hardening behavior in tension and compression, the post-yield tensile resistance is significantly greater than the compressive resistance. At a loading displacement of 22 mm, the peak tensile strength is approximately 1.47 times the peak compressive strength.

3.3.3. Self-centering behavior

Fig. 13(a) illustrates the residual displacements of the SMA-Ω damper under different loading amplitudes. As the loading displacement increases, the residual deformation gradually increases. However, the maximum residual deformation remains limited to only 1.48 mm. Fig. 13(b) shows the deformation recovery ratio of the SMA-Ω damper at each loading amplitude, defined as the difference between the maximum deformation and the residual deformation, normalized by the maximum deformation. As observed in Fig. 13(b), the deformation recovery ratio exceeds 93%, confirming the excellent deformation recovery capability (i.e., self-centering ability) of the SMA-Ω damper upon unloading. This superior self-centering performance highlights the significant potential of the SMA-Ω damper in enhancing the seismic resilience of structural systems.

3.3.4. Energy-dissipation capacity

Fig. 14 presents the equivalent damping ratios of the SMA-Ω damper under various loading amplitudes. The equivalent damping ratio is calculated using Eq. (24). As shown in Fig. 14, once the SMA-Ω damper yields, its equivalent damping ratio increases progressively with the loading displacement, demonstrating a stable energy-dissipation capacity. The maximum equivalent damping ratio reaches 8.08%. Although the equivalent damping ratio of the SMA-Ω damper is smaller than that of conventional steel dampers, it provides superior self-centering capability. According to the related studies by Hu et al. [30,77], the damping of SMA components can be effectively enhanced by incorporating parallel viscous or viscoelastic dampers without compromising their self-centering performance.

$$\xi_e = \frac{E_d}{2\pi E_e} \tag{24}$$

in which E_d is the hysteretic energy dissipation in one cycle, and E_e is the elastic strain energy stored in the equivalent linear system with the secant stiffness determined at the peak displacement.

4. Numerical investigation

4.1. Numerical modeling and validation

To gain deeper insight into the stress–strain states of the SMA-Ω damper under external loading and to investigate the influence of key design parameters on its mechanical performance, numerical analyses were conducted using ABAQUS [78] in this section. Fig. 15 illustrates the 3D solid finite element model of the SMA-Ω damper developed in ABAQUS. All components were modeled using C3D8R solid elements. The superelastic behavior of SMA was defined using the superelastic material model available in ABAQUS, and the key material parameters are summarized in Table 2.

The steel components were modeled using a bilinear kinematic hardening material model. The interactions between all components were defined using surface-to-surface contact. The normal contact behavior was specified as hard contact with no penetration, while the tangential behavior was modeled using a penalty friction formulation with a friction coefficient of 0.3. Fig. 15 also illustrates the meshing strategy adopted in the finite element model. Since the connecting components remain elastic throughout the loading process, relatively

(a) compression (b) tension

Fig. 11. deformation mechanism.

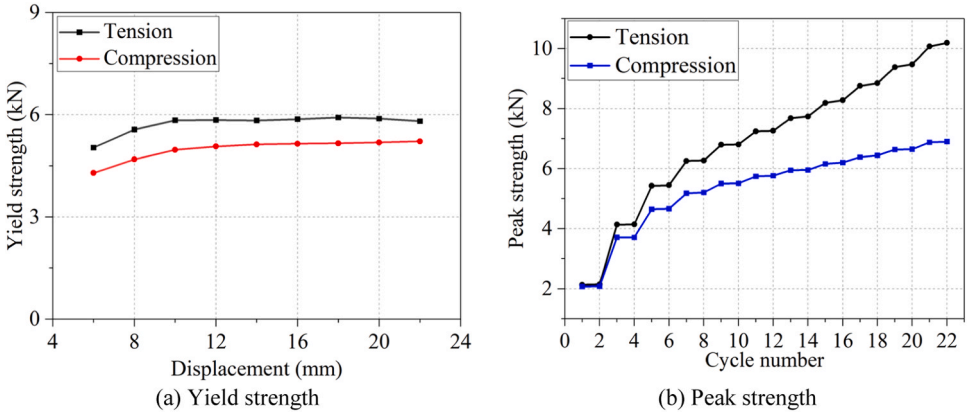

Fig. 12. Strength of the tested SMA-Ω damper.

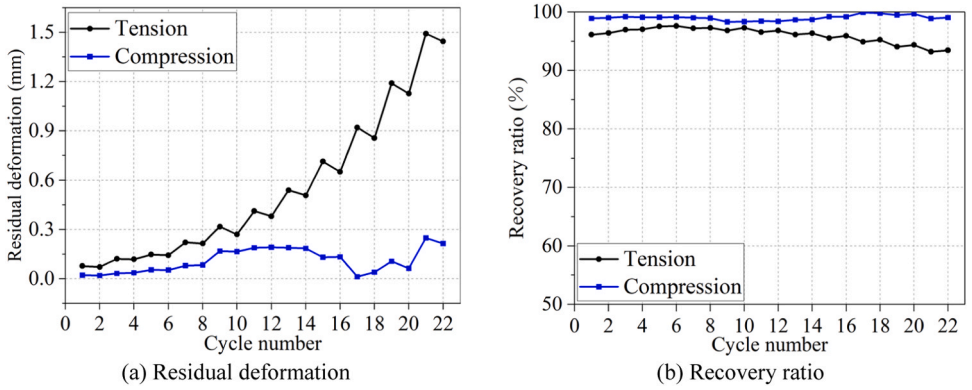

Fig. 13. Residual deformation and recovery ratio.

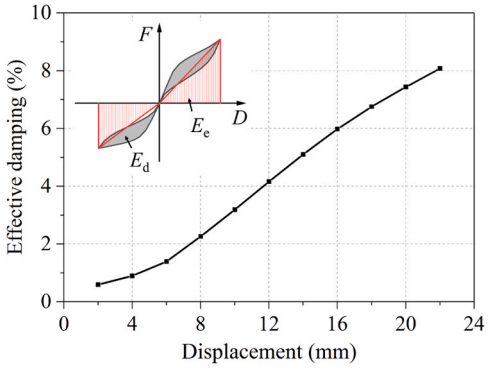

Fig. 14. Equivalent damping ratio.

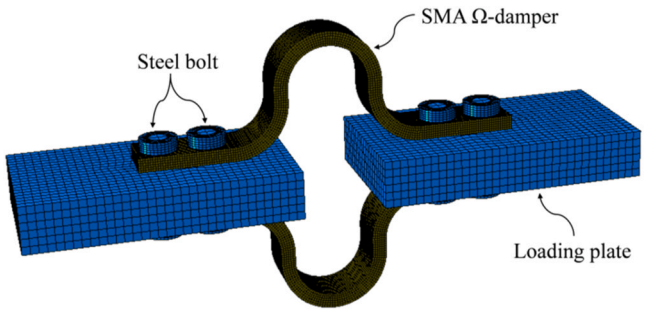

Fig. 15. Numerical model of the SMA-Ω damper.

Table 2
Parameters for defining the superelastic material model.

Definition	Parameter	Value
Young's modulus of austenite	E_A	55.0 GPa
Young's modulus of martensite	E_M	26.0 GPa
Start of transformation stress in loading under tension	σ_{MS}	325.0 MPa
End of transformation stress in loading under tension	σ_{Mf}	500.0 MPa
Start of transformation stress in unloading under tension	σ_{AS}	350.0 MPa
End of transformation stress in unloading under tension	σ_{Af}	50.0 MPa
Start of transformation stress in loading under compression	$\sigma_{MS,com}$	325.0 MPa
Maximum transformation strain	ε_l	2.5%
Poisson's ratio of austenite	ν_A	0.33
Poisson's ratio of martensite	ν_M	0.33

small mesh sizes were assigned to these regions. In contrast, finer mesh elements were used for the SMA-Ω damper and the bolts. In particular, six mesh layers were generated through the thickness of the SMA-Ω damper to accurately capture the stress and strain distributions across its cross-section.

Fig. 16 compares the finite element (FE) predictions with the experimental hysteresis curves. The FE model exhibits excellent agreement with the test results and accurately captures the tensile–compressive loading and unloading behavior of the SMA-Ω damper, thereby confirming the validity of the adopted modeling approach. Fig. 17 presents the maximum principal strain distribution of the SMA-Ω damper during tension and compression, providing a clear visualization of the martensitic phase transformation process in SMA under loading. Unlike SMA bars or wires subjected to axial loading, which typically exhibit uniform strain fields, the strain in the SMA-Ω damper is highly localized. Three critical regions experience the highest strains: (i) the

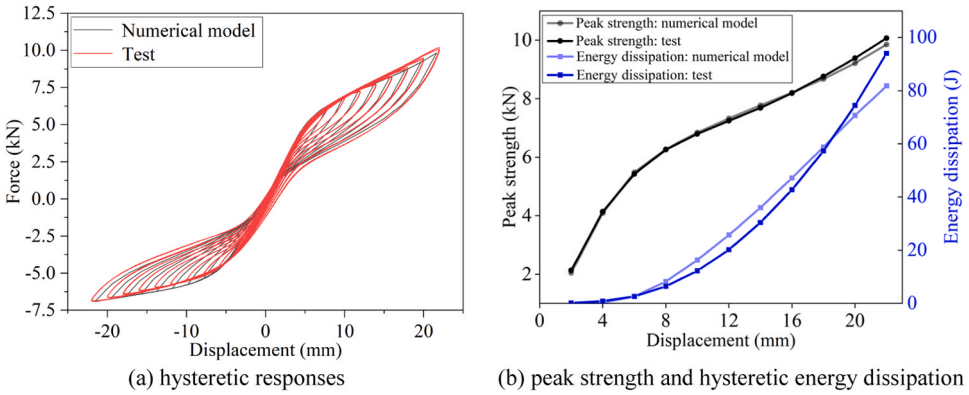

(a) hysteretic responses (b) peak strength and hysteretic energy dissipation

Fig. 16. Validation of the numerical model.

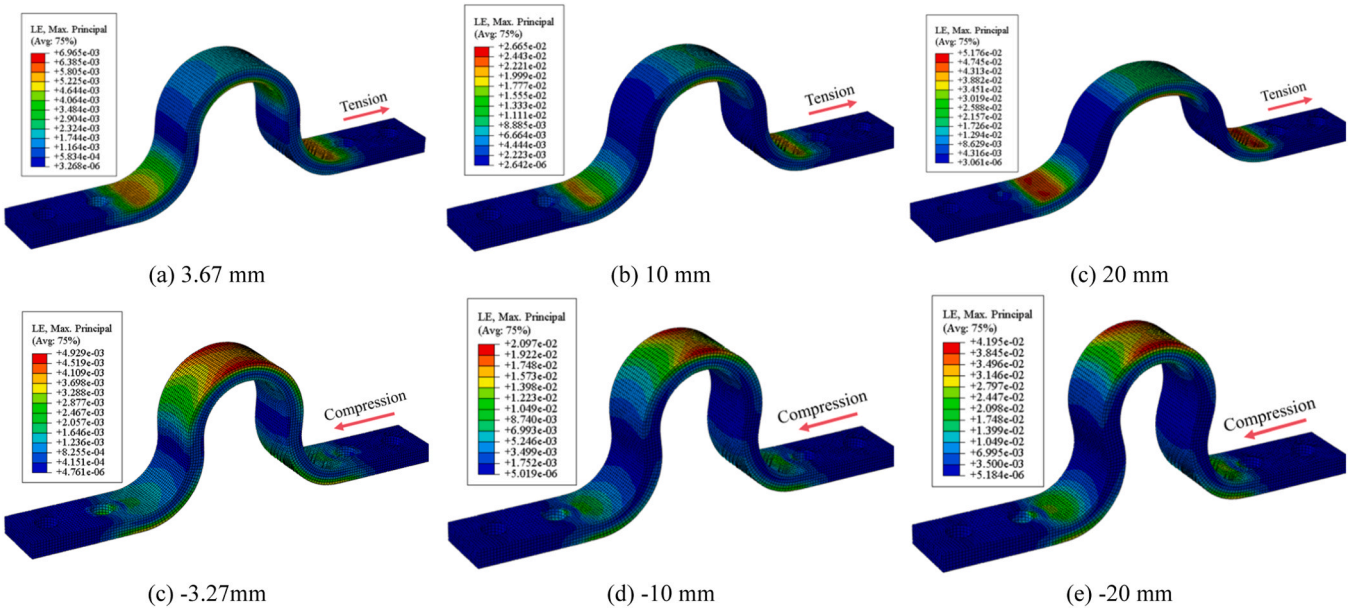

(a) 3.67 mm (b) 10 mm (c) 20 mm

(c) -3.27mm (d) -10 mm (e) -20 mm

Fig. 17. Maximum principal strain distribution of the SMA-Ω damper.

top of the U-shaped segment, and (ii) the areas where the quarter-circle plates come into contact with the bolts. As shown in Fig. 17(a), at a loading displacement of 3.67 mm, the maximum principal strains at the top of the U-shaped segment and at the bolt–plate contact regions reach 0.70% and 0.49%, respectively, indicating the onset of the austenite-to-martensite transformation in these regions. The maximum principal strain distributions across the cross-section further demonstrate a pronounced non-uniformity: the strain at the outer fibers is significantly larger than that at the inner fibers. As the loading displacement increases, the strain level rises accordingly. When the SMA enters the transformation phase (i.e., after starting the phase transformation from austenite to martensite), the strain distribution during tension and compression begins to differ significantly. For example, at a displacement of 10 mm, the maximum cross-sectional strain under tension is 2.67%, which is greater than that under compression (i.e., 2.10%) due to the different deformation modes. This difference in local strain evolution explains the macroscopic behavior in which the tensile strength of the SMA-Ω damper exceeds its compressive strength.

Table 3
The specific parameters considered in the parametric analysis.

Component Name	t (mm)	R (mm)	r (mm)	d_1 (mm)
SMAΩ1	6	20	20	0
SMAΩ2	6	20	20	10
SMAΩ3	6	20	20	15
SMAΩ4	6	20	5	5
SMAΩ5	6	20	10	5
SMAΩ6	6	20	15	5
SMAΩ7	4	20	20	5
SMAΩ8	8	20	20	5
SMAΩ9	10	20	20	5
SMAΩ10	6	20	20	5
SMAΩ11	6	25	20	5
SMAΩ12	6	30	20	5
SMAΩ13	6	40	20	5

4.2. Parametric simulations

Parametric numerical analyses were conducted in this section to investigate the influence of key design parameters (including t, R, r, and d_1) on the nonlinear behavior of the SMA-Ω damper. The specific parameters considered in the parametric analysis are summarized in Table 3. The variation ranges of the geometric parameters in the parametric study were selected primarily to investigate their influence patterns on the damper behavior. For each parameter, four representative values were considered to capture both the overall trend and the possible nonlinear effects of parameter variation within a reasonable

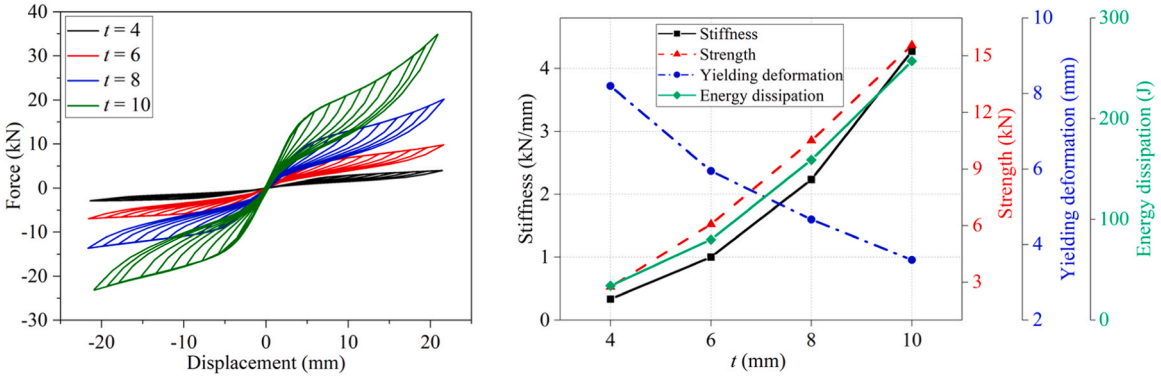

(a) hysteretic responses (b) stiffness, strength, and yielding deformation

Fig. 18. Influence of *t*.

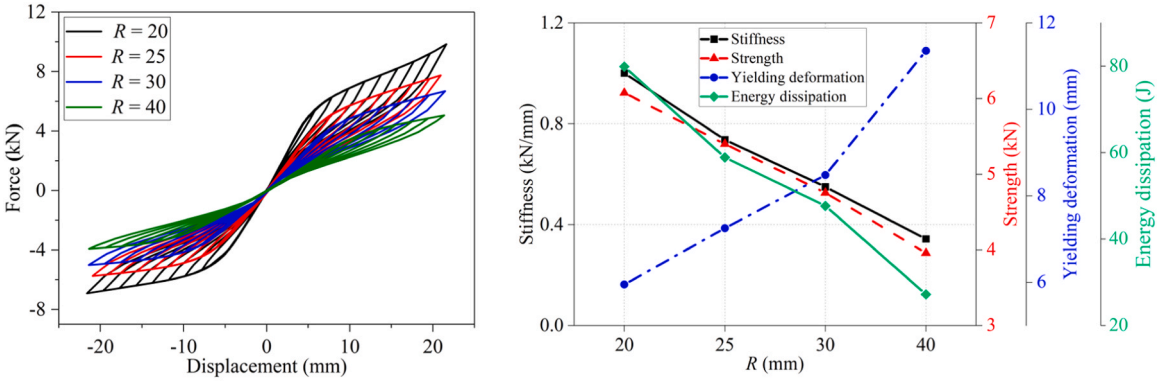

(a) hysteretic responses (b) stiffness, strength, and yielding deformation

Fig. 19. Influence of *R*.

range. It should be noted that these parameter ranges were intended for sensitivity analysis rather than to define strict theoretical limits.

Fig. 18(a) presents the hysteresis curves of the SMA-Ω damper for thicknesses $t = 4$, 6, 8, and 10 mm, with $R = 20$ mm, $r = 20$ mm, and $d_1 = 5$ mm. As shown in the figure, the thickness t has a pronounced influence on the stiffness, strength, and energy-dissipation capacity of the SMA-Ω damper. Fig. 18(b) illustrates that, as t increases, both the initial stiffness and the yield strength progressively increase, whereas the yield displacement decreases. This trend arises because, for a given section rotation, a larger cross-sectional height results in higher strain at the outer fibers, causing strain development to proceed more rapidly in thicker sections. It is noteworthy that when $t = 10$ mm, the SMA-Ω damper exhibits a pronounced hardening behavior in tension once the displacement exceeds 15 mm, which is attributed to martensitic hardening of the SMA material. These findings indicate that increasing the thickness effectively enhances the lateral stiffness and load-carrying capacity of the SMA-Ω damper but may also lead to premature martensitic hardening behavior.

Fig. 19(a) illustrates the influence of the semicircular radius R of the U-shaped segment on the hysteretic behavior of the SMA-Ω damper, where $t = 6$ mm, $r = 20$ mm, and $d_1 = 5$ mm. As shown, the radius R has a clear and systematic effect on the stiffness, strength, and energy-dissipation characteristics of the damper. As shown in Fig. 19(b), when R increases from 20 mm to 40 mm, the overall stiffness and peak

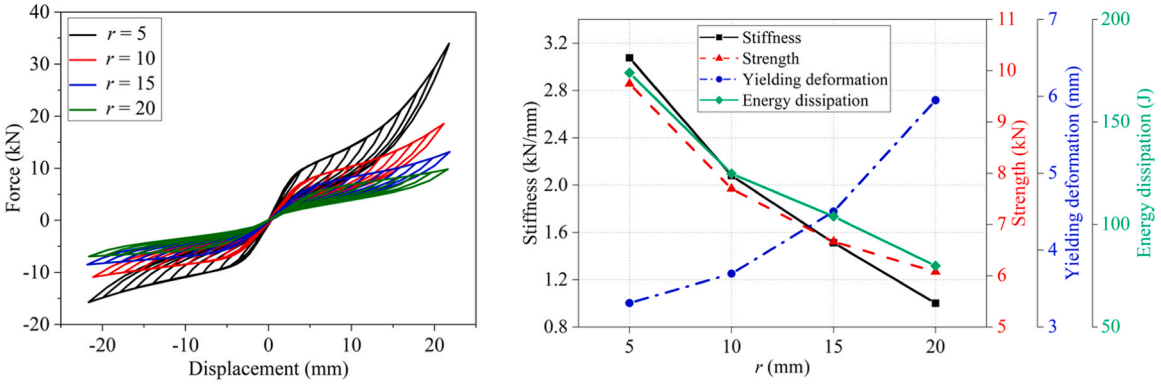

(a) hysteretic responses (b) stiffness, strength, and yielding deformation

Fig. 20. Influence of *r*.

strength decrease noticeably. This is because a larger radius reduces the curvature of the U-shaped segment, effectively lowering the bending stiffness and decreasing the strain demand at the critical curved regions for a given displacement. Consequently, the forward transformation of SMA occurs more gradually, leading to a smoother and less steep hardening branch. For $R = 20$ mm, the damper exhibits the highest initial stiffness and peak strength, along with the largest energy-dissipation capacity, as evidenced by the wider hysteresis loops. When $R = 40$ mm, the loops become significantly narrower, indicating reduced energy dissipation and a more compliant global response. The results demonstrate that a smaller semicircular radius promotes higher curvature, larger local strains, and earlier martensitic transformation, thereby enhancing both stiffness and strength. In contrast, increasing R weakens the mechanical performance but is expected to improve deformability due to reduced strain concentration, which is evidenced by the increasing yielding deformation (see Fig. 19(b)).

Fig. 20(a) illustrates the effect of the quarter-circle plate radius r on the hysteretic behavior of the SMA-Ω damper, where $t = 6$ mm, $R = 20$ mm, and $d_1 = 5$ mm. The radius r significantly influences the local curvature and bending stiffness of the transition region, which in turn affects the stiffness, strength, and energy-dissipation capacity of the damper. As shown in Fig. 20(b), decreasing r leads to a substantial increase in both the initial stiffness and the peak strength. This is because a smaller radius produces higher curvature at the quarter-circle plates, inducing larger local strains for the same global displacement and thereby accelerating the martensitic transformation of SMA. When $r = 5$ mm, the damper exhibits the highest stiffness, largest peak force, and the widest hysteresis loops, indicating superior energy-dissipation capacity. In contrast, for $r = 20$ mm, the response becomes noticeably softer, and the hysteresis loops narrow considerably, reflecting reduced energy dissipation and delayed phase transformation. The progressive reduction in stiffness and strength with increasing r demonstrates that the geometry of the curved transition region plays a critical role in controlling the strain development within the SMA material. Similar to the influence of R, reducing the radius r may also degrade the deformation capacity of the SMA-Ω damper. This trend is reflected in the decreasing yield displacement observed as r becomes smaller (see Fig. 20(b)). A smaller radius induces higher curvature and localized strains at the quarter-circle plates, which can trigger earlier phase transformation and martensitic hardening, thereby limiting the overall deformation capacity of the component.

Fig. 21(a) shows the effect of the connecting length d_1 between the U-shaped segment and the quarter-circle plates on the hysteretic behavior of the SMA-Ω damper, where $t = 6$ mm, $R = 20$ mm, and $r = 20$ mm. Increasing d_1 effectively increases the overall height of the damper, thereby reducing the curvature demand in the transition region for a given global displacement. As shown in Fig. 21(b), the SMA-Ω damper exhibits progressively lower stiffness, peak strength, and energy-dissipation capacity as d_1 increases from 0 mm to 15 mm. When $d_1 = 0$ mm, the hysteresis loops are the widest, demonstrating the highest energy dissipation and the most pronounced martensitic transformation. In contrast, for $d_1 = 15$ mm, the loops become noticeably narrower, indicating a softer global response and reduced energy dissipation. The reduction in mechanical performance with increasing d_1 can be attributed to the redistribution of deformation along a taller structural profile. A larger d_1 lowers the strain concentration in the curved regions and delays the initiation of the austenite-to-martensite transformation, resulting in decreased stiffness and peak strength. In addition, as shown in Fig. 21(b), the yield displacement increases with increasing d_1, reflecting the lower curvature-induced strain for the same global displacement, which is beneficial in enhancing deformability.

4.3. Design recommendation

Fig. 22 compares the stiffness and yield strength predicted by the theoretical formulations in Section 2 with those obtained from the finite element analyses and tests. As shown in Fig. 22(a), Eq. (17) predicts the initial stiffness of the SMA-Ω damper with good accuracy, yielding an average error of 3.6%. However, Fig. 22(b) shows that the yield strength calculated using Eq. (23) differs considerably from the yield strength obtained from both the experiments and FE analyses. Two primary reasons account for this discrepancy: (1) Eq. (23) calculates the force corresponding to the onset of the austenite-to-martensite transformation, whereas in engineering design, the yield strength is typically defined as the force at the noticeable turning point on the force–displacement curve, at which most of the cross-sectional fibers in SMA-Ω damper have already stared the phase transformation from austenite to martensite; and (2) Eq. (23) is derived based on the small-deformation assumption, while the actual yield displacement of the SMA-Ω damper is relatively large, making the small-deformation approximation insufficient. To address these issues, a strength modification factor λ is introduced to Eq. (23). Accordingly, the engineering yield strength of the SMA-Ω damper can be evaluated using Eq. (25). Based on the experimental and FE results, the modification factor λ is taken as 1.96 in tension and 1.78 in compression. Fig. 23 presents the comparison between the yield strength predicted by Eq. (25) and the experimental and FE results. The modified formulation provides a significantly improved prediction, with an average error of only 3.2%, confirming its suitability for engineering design of SMA-Ω dampers.

$$F_y = \lambda \frac{bt^2 \sigma_{Ms}}{\sqrt{3}(r + d_1 + R)} \tag{25}$$

5. Conclusions

This paper developed a novel SMA-Ω damper as a new self-centering

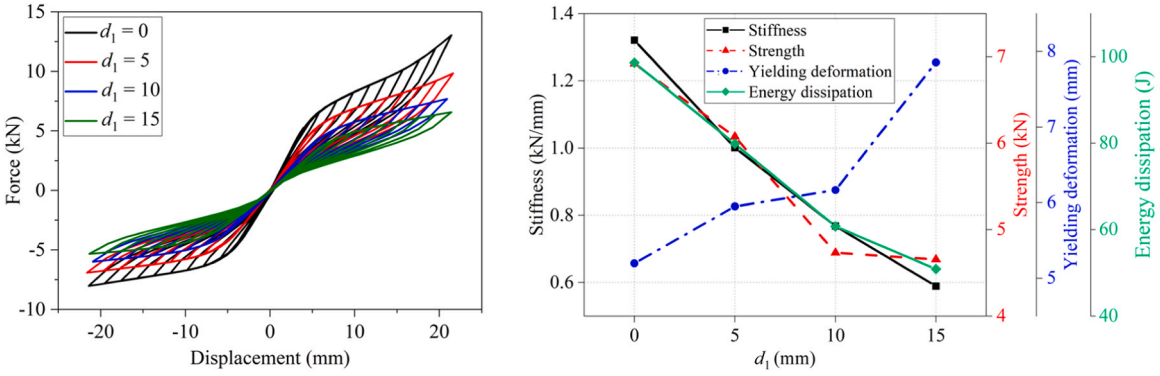

(a) hysteretic responses (b) stiffness, strength, and yielding deformation

Fig. 21. Influence of d_1.

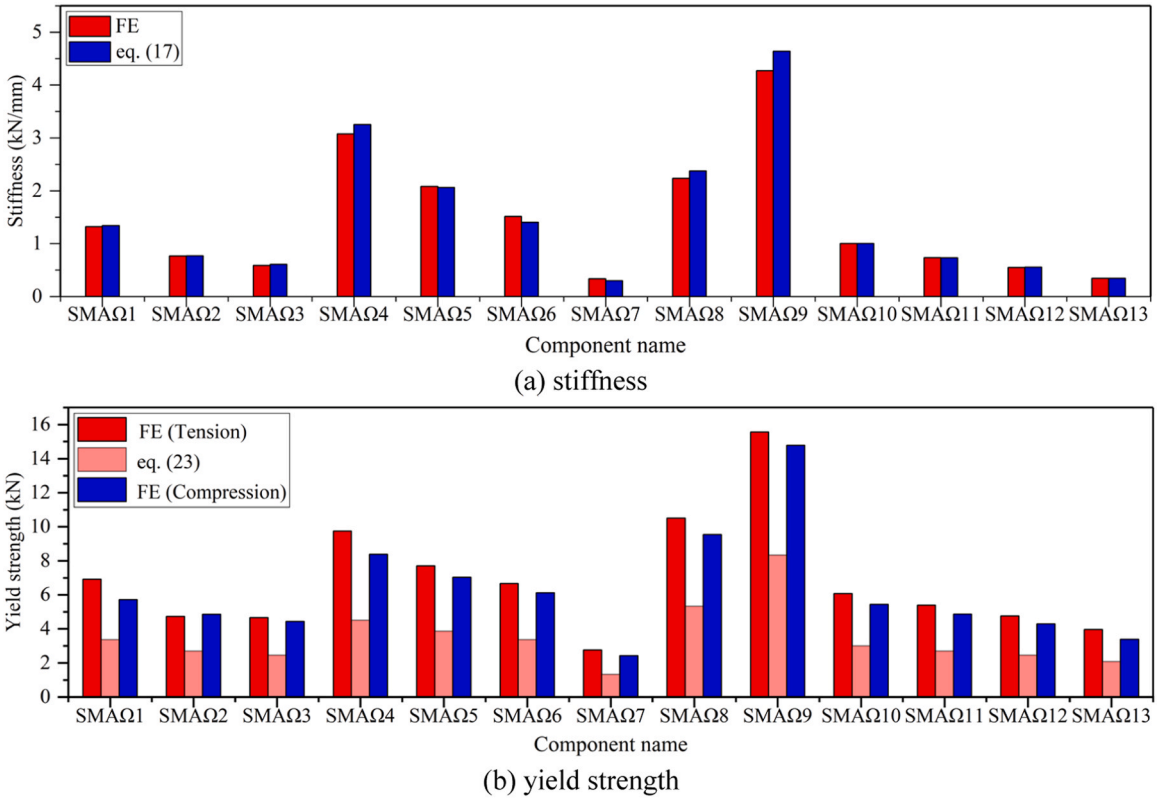

Fig. 22. Comparison between the results from the theoretical formulations and that from the finite element analyses.

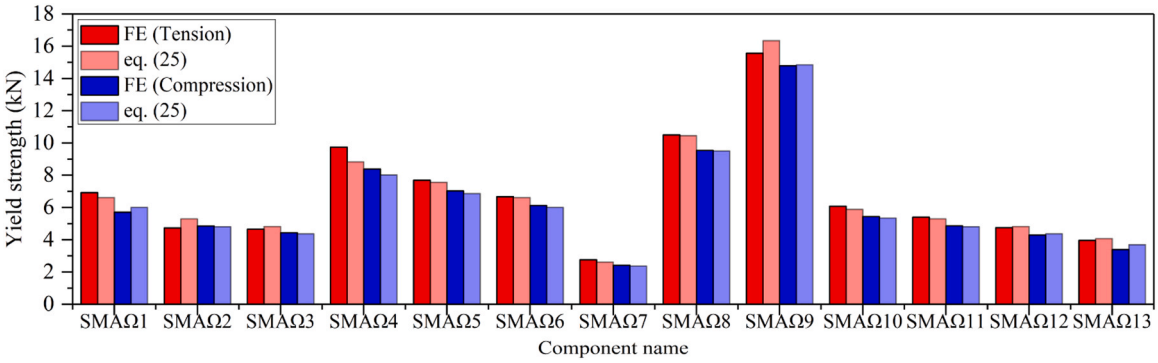

Fig. 23. Comparison between the results from Eq. (25) and those from the finite element analyses.

component for developing seismic resilient engineering structures. The theoretical mechanical behavior of the proposed SMA-Ω damper was analyzed. Validation tests and parametric numerical simulations were conducted to investigate its nonlinear behavior. The major conclusions are summarized as follows:

- The SMA-Ω damper provides stable flag-shaped hysteresis with negligible residual deformation and reliable recovery ratios exceeding 93% under cyclic loading, demonstrating strong potential for seismic resilience-oriented design.
- The SMA-pi damper eventually fractured at the circular transition between the flat and U-shaped segments, where stress concentration was the most severe. In contrast, the SMA-Ω damper fractured at the top of the U-shaped segment, indicating a more desirable failure mode. Owing to the improved geometric configuration, the SMA-Ω damper effectively alleviated stress concentration and achieved markedly enhanced deformation capacity, with a ductility ratio of 3.90, which was 1.25 times that of the SMA-pi damper.
- Parametric analyses reveal that the geometric parameters t, R, r, and d_1 govern stiffness, strength, and strain distribution. Larger thickness (t), smaller radii (R, r), and shorter transition lengths (d_1) increase stiffness, strength, and energy-dissipation capacity but may induce stress concentration and reduce deformation capacity. Conversely, smaller t and larger R, r, and d_1 improve deformability but reduce stiffness, strength, and energy dissipation.
- The developed initial stiffness prediction formula (i.e., Eq. 17) and the adjusted yield-strength expression (i.e., Eq. 24) can accurately predict the initial stiffness and yield strength of the proposed SMA-Ω damper in both tension and compression, with an average error lower than 3.2%.

6. Limitations and future work

It should be noted that the influence of ambient temperature on the behavior of the proposed SMA damper was not explicitly considered in the present study. Since SMA materials are sensitive to temperature

variations, especially under low-temperature conditions where their superelastic behavior may deteriorate, the self-centering performance of the damper may be affected accordingly. Therefore, the findings of this study should be interpreted within the investigated temperature range and loading conditions. Future research should systematically examine the thermo-mechanical behavior of the proposed damper under different ambient temperatures, with particular attention to its energy dissipation capacity, deformation recovery ability, and overall self-centering performance.

The proposed correction coefficient values (i.e., λ in Eq. (25)) were derived based on the present parametric analysis and are applicable only within the investigated ranges of geometric parameters considered in this study. If the adopted parameters fall outside these ranges, further validation is required.

The damper specimens tested in the present study were relatively small in size. Although the obtained results provide useful insight into the mechanical behavior of the proposed damper, the performance of larger-scale dampers should be further investigated to meet the demands of different application scenarios.

The objective of this study is to propose a new bending-type SMA component and investigate its nonlinear behavior and mechanical characteristics, rather than to carry out a systematic comparative evaluation with other existing bending-type SMA components. Such a comparison is meaningful and will be considered in future work.

The present study mainly focuses on the global mechanical behavior of the proposed SMA-Ω damper, including its hysteretic response, load-carrying capacity, self-centering capability, energy dissipation capacity, and deformation capacity. More detailed investigation of local failure characteristics, such as fracture initiation and propagation, local yielding zones, and martensitic transformation evolution, requires dedicated experimental measurements and is beyond the scope of this study. Future work should address these aspects through more comprehensive testing and local response monitoring.

The present experimental program was primarily conducted as a validation-oriented study to verify the feasibility and fundamental mechanical behavior of the proposed SMA-Ω damper. The variability and uncertainty among test specimens were not considered. A rigorous evaluation of specimen-to-specimen scatter would require a larger number of repeated tests and statistical analysis, which is beyond the scope of the present study. Future work should further examine the uncertainty and variability of damper behavior through more extensive experimental investigations.

CRediT authorship contribution statement

Shuling Hu: Writing – original draft, Validation, Supervision, Resources, Project administration, Methodology, Investigation, Funding acquisition, Conceptualization. **Jinmeng Zang:** Visualization, Validation, Software, Investigation, Formal analysis, Data curation. **Tong Guo:** Writing – review & editing, Validation, Supervision, Resources, Project administration, Funding acquisition. **Zhi-Peng Chen:** Writing – review & editing, Validation, Supervision, Resources, Investigation. **Theodoros L. Karavasilis:** Writing – review & editing, Validation, Supervision, Resources, Methodology. **M. Shahria Alam:** Writing – review & editing, Validation, Supervision. **Vasileios C. Kamperidis:** Writing – review & editing, Validation.

Declaration of Competing Interest

The authors declare that they have no known competing financial interests or personal relationships that could have appeared to influence the work reported in this paper.

Acknowledgment

The financial support provided by the National Natural Science Foundation of China (Grant Nos. 52508163 and 52125802), the Basic Research Program of Jiangsu (Grant No. BK20251277), and the European Union's Marie Skłodowska-Curie Actions (Grant No. 101146673) is gratefully acknowledged.

Data availability

Data will be made available on request.

References

[1] X. He, Y. Tajiri, S. Unjoh, S. Yamazaki, T. Noro, Experimental study of a scaled bridge model with a unidirectional rocking isolation bearing system (Uni-RIBS) through shaking table tests, Earthq. Eng. Struct. Dyn. 53 (2024) 3054–3070.
[2] Y. Lin, X. He, A. Igarashi, Influence of directionality of spectral-compatible Bi-directional ground motions on critical seismic performance assessment of base-isolation structures, Earthq. Eng. Struct. Dyn. 51 (2022) 1477–1500.
[3] 2013 CEN.
[4] Code for seismic design of buildings (GB 50011-2010) 2010 China Architecture & Building Press, Beijing.
[5] ASCE, ASCE/SEI 7-16. Minimum design loads for buildings and other structures, American Society of Civil Engineers,, Reston VA, 2016.
[6] J. Men, G. Chen, Multi-hazard coupling fragility analysis for steel cylindrical tanks subjected to earthquake-tsunami sequence, Reliab. Eng. Syst. Saf. 269 (2026) 112041.
[7] X. Li, J. Wen, Z. Ye, H. Liang, Y. Wei, Seismic resilience evaluation for substations considering diversity of earthquake sources, Reliab. Eng. Syst. Saf. 270 (2026) 112163.
[8] S. Liu, O. Chen, Y. Liao, S. Zeng, S. Hu, Prediction of the overstrength for ordinary shear links in eccentrically braced frames, Struct. Elsevier (2026) 110958.
[9] K. Ke, Y. Chen, X. Zhou, M.C. Yam, S. Hu, Experimental and numerical study of a brace-type hybrid damper with steel slit plates enhanced by friction mechanism, Thin-Walled Struct. 182 (2023) 110249.
[10] J. Hu, C. Zhai, W. Wen, Rapid post-earthquake functionality prediction of subway systems based on graph neural networks and attentive transfer learning, Reliab. Eng. Syst. Saf. 270 (2026) 112146.
[11] Y. Lin, Y. Fu, J. Sun, R. Xie, X. He, Robust seismic response evaluation considering an uncertainty emerging in asymmetric bridges, Reliab. Eng. Syst. Saf. 266 (2025) 111740.
[12] L.A. Fahnestock, R. Sause, J.M. Ricles, Seismic response and performance of buckling-restrained braced frames, J. Struct. Eng. 133 (2007) 1195–1204.
[13] J. Erochko, C. Christopoulos, R. Tremblay, H. Choi, Residual drift response of SMRFs and BRB frames in steel buildings designed according to ASCE 7-05, J. Struct. Eng. 137 (2010) 589–599.
[14] FEMA, FEMA P58. Seismic performance assessment of buildings, Federal Emergency Management Agency,, 2012.
[15] A. Wood, I. Noy, M. Parker, The Canterbury rebuild five years on from the Christchurch earthquake, Reserve Bank N. Z. Bull. 79 (2016) 1–16.
[16] S. Hu, S. Zhu, M.S. Alam, W. Wang, Machine learning-aided peak and residual displacement-based design method for enhancing seismic performance of steel moment-resisting frames by installing self-centering braces, Eng. Struct. 271 (2022) 114935.
[17] S. Hu, S. Zhu, W. Wang, Machine learning-driven probabilistic residual displacement-based design method for improving post-earthquake repairability of steel moment-resisting frames using self-centering braces, J. Build. Eng. 61 (2022) 105225.
[18] S. Hu, S. Liu, S. Zeng, B. Zhang, Z. Xu, Investigating seismic performance of a novel self-centering shear link in EBF utilizing experimental and numerical simulation, J. Constr. Steel Res. 224 (2025) 109129.
[19] S. Kitayama, M.C. Constantinou, Probabilistic collapse resistance and residual drift assessment of buildings with fluidic self-centering systems, Earthq. Eng. Struct. Dyn. 45 (2016) 1935–1953.
[20] Z. Liu, C. Zhang, X. Ran, W. Zhao, A. Guo, Long-term resilience assessment of bridge networks using data-driven seismic analysis method for deteriorating bridges, Reliab. Eng. Syst. Saf. 268 (2026) 112048.
[21] X. He, S. Unjoh, T. Makino, C. Nagao, A. Shibasaki, T. Noro, et al., Structural health monitoring of a unidirectional isolation bridge: Bidirectional seismic behavior, stochastic model updating, and prediction, Earthquake Engineering & Structural Dynamics,, 2025.
[22] S. Hu, W. Wang, M.S. Alam, K. Ke, Life-cycle benefits estimation of self-centering building structures, Eng. Struct. 284 (2023) 115982.
[23] S. Hu, S. Zhu, Life-cycle benefits estimation for hybrid seismic-resistant self-centering braced frames, Earthq. Eng. Struct. Dyn. (2023) 1–23.
[24] R. DesRoches, J. McCormick, M. Delemont, Cyclic properties of superelastic shape memory alloy wires and bars, J. Struct. Eng. 130 (2004) 38–46.
[25] S. Hu, Y. Koetaka, Z.-P. Chen, S. Zhu, M.S. Alam, Hybrid self-centering braces with NiTi-SMA U-shaped and frequency-dependent viscoelastic dampers for structural and nonstructural damage control, Eng. Struct. 308 (2024) 117920.
[26] S. Zhu, Y. Zhang, Seismic analysis of concentrically braced frame systems with self-centering friction damping braces, J. Struct. Eng. 134 (2008) 121–131.
[27] S. Zhu, Y. Zhang, A thermomechanical constitutive model for superelastic SMA wire with strain-rate dependence, Smart Mater. Struct. 16 (2007) 1696.

[28] C.-X. Qiu, S. Zhu, Performance-based seismic design of self-centering steel frames with SMA-based braces, Eng. Struct. 130 (2017) 67–82.
[29] C. Qiu, S. Zhu, Shake table test and numerical study of self-centering steel frame with SMA braces, Earthq. Eng. Struct. Dyn. 46 (2017) 117–137.
[30] S. Hu, C. Qiu, S. Zhu, Machine learning-driven performance-based seismic design of hybrid self-centering braced frames with SMA braces and viscous dampers, Smart Mater. Struct. 31 (2022) 105024.
[31] F.H. Dezfuli, M.S. Alam, Shape memory alloy wire-based smart natural rubber bearing, Smart Mater. Struct. 22 (2013) 045013.
[32] G. Zhou, P. Lloyd, Design, manufacture and evaluation of bending behaviour of composite beams embedded with SMA wires, Compos. Sci. Technol. 69 (2009) 2034–2041.
[33] O.E. Ozbulut, S. Daghash, M.M. Sherif, Shape memory alloy cables for structural applications, J. Mater. Civ. Eng. 28 (2016) 04015176.
[34] C. Fang, Y. Zheng, J. Chen, M.C. Yam, W. Wang, Superelastic NiTi SMA cables: thermal-mechanical behavior, hysteretic modelling and seismic application, Eng. Struct. 183 (2019) 533–549.
[35] F. Shi, O.E. Ozbulut, Z. Li, Z. Wu, F. Ren, Y. Zhou, Effects of ambient temperature on cyclic response and functional fatigue of shape memory alloy cables, J. Build. Eng. 52 (2022) 104340.
[36] F. Shi, Y. Zhou, O.E. Ozbulut, F. Ren, Hysteretic response and failure behavior of an SMA cable-based self-centering brace, Struct. Control Health Monit. 29 (2022) e2847.
[37] F. Shi, Y. Zhou, A. Erbolat, Q. Li, C. Zhang, L. Sun, Effects of training strategy on the mechanical behavior of shape memory alloy cable brace, J. Build. Eng. (2025) 115052.
[38] S. Cao, O.E. Ozbulut, F. Shi, J. Deng, An SMA cable-based negative stiffness seismic isolator: development, experimental characterization, and numerical modeling, J. Intell. Mater. Syst. Struct. 33 (2022) 1819–1833.
[39] S. Li, F.H. Dezfuli, J.-Q. Wang, M.S. Alam, Displacement-based seismic design of steel, FRP, and SMA cable restrainers for isolated simply supported bridges, J. Bridge Eng. 23 (2018) 04018032.
[40] B. Mas, D. Biggs, I. Vieito, A. Cladera, J. Shaw, F. Martínez-Abella, Superelastic shape memory alloy cables for reinforced concrete applications, Constr. Build. Mater. 148 (2017) 307–320.
[41] W. Wang, C. Fang, J. Liu, Large size superelastic SMA bars: heat treatment strategy, mechanical property and seismic application, Smart Mater. Struct. 25 (2016) 075001.
[42] Z.-P. Chen, S. Zhu, Novel two-stage superelastic SMA bars with enhanced ductility and graded pseudo-yielding for seismic applications, Eng. Struct. 294 (2023) 116727.
[43] N. Rahgozar, M.S. Alam, Functional recovery evaluation of hybrid self-centering piston-based braced frames, Earthq. Eng. Struct. Dyn. (2023).
[44] C. Fang, W. Wang, C. He, Y. Chen, Self-centring behaviour of steel and steel-concrete composite connections equipped with NiTi SMA bolts, Eng. Struct. 150 (2017) 390–408.
[45] H.R. Azariani, M.R. Esfahani, H. Shariatmadar, Behavior of exterior concrete beam-column joints reinforced with Shape Memory Alloy (SMA) bars. Steel and composite structures, Int. J. 28 (2018) 83–98.
[46] Z.P. Chen, S. Zhu, Development of a novel shape memory alloy-based self-centering precast segmental concrete column, Struct. Control Health Monit. 29 (2022) e3099.
[47] A.M. Billah, M.S. Alam, Seismic performance of concrete columns reinforced with hybrid shape memory alloy (SMA) and fiber reinforced polymer (FRP) bars, Constr. Build. Mater. 28 (2012) 730–742.
[48] H. Rojob, R. El-Hacha, Performance of RC beams strengthened with self-prestressed Fe-SMA bars exposed to freeze-thaw cycles and sustained load, Eng. Struct. 169 (2018) 107–118.
[49] M.S. Alam, M.R. Bhuiyan, A.M. Billah, Seismic fragility assessment of SMA-bar restrained multi-span continuous highway bridge isolated by different laminated rubber bearings in medium to strong seismic risk zones, Bull. Earthq. Eng. 10 (2012) 1885–1909.
[50] B. Wang, S. Zhu, Seismic behavior of self-centering reinforced concrete wall enabled by superelastic shape memory alloy bars, Bull. Earthq. Eng. 16 (2018) 479–502.
[51] X. Zhou, Y. Huang, K. Ke, M.C. Yam, H. Zhang, H. Fang, Large-size shape memory alloy plates subjected to cyclic tension: towards novel self-centring connections in steel frames, Thin-Walled Struct. 185 (2023) 110591.
[52] X. Zhou, K. Ke, M.C. Yam, Q. Zhao, Y. Huang, J. Di, Shape memory alloy plates: cyclic tension-release performance, seismic applications in beam-to-column connections and a structural seismic demand perspective, Thin-Walled Struct. 167 (2021) 108158.
[53] S. Moradi, M.S. Alam, Feasibility study of utilizing superelastic shape memory alloy plates in steel beam–column connections for improved seismic performance, J. Intell. Mater. Syst. Struct. 26 (2015) 463–475.
[54] N.M. Mirzai, H.M. Cho, J.W. Hu, Experimental study of new axial recentering dampers equipped with shape memory alloy plates, Struct. Control Health Monit. 28 (2021) e2680.
[55] B. Wang, S. Zhu, Cyclic tension–compression behavior of superelastic shape memory alloy bars with buckling-restrained devices, Constr. Build. Mater. 186 (2018) 103–113.
[56] C. Qiu, C. Fang, D. Liang, X. Du, M.C. Yam, Behavior and application of self-centering dampers equipped with buckling-restrained SMA bars, Smart Mater. Struct. 29 (2020) 035009.
[57] C. Qiu, T. Jiang, J. Liu, X. Du, Seismic performance of knee-braced frames equipped with NiTi BRBs, J. Constr. Steel Res. 197 (2022) 107480.
[58] C. Qiu, J. Liu, X. Du, Analytical and numerical study on the cyclic behavior of buckling-restrained SMA-based self-centering damper, Smart Mater. Struct. 30 (2021) 095021.
[59] X. Zhou, B. Han, K. Ke, J. Di, F. Qin, L. Hu, Experimental study of shape memory alloy plates under cyclic tension–compression loading scenarios, Eng. Struct. 297 (2023) 117002.
[60] B. Wang, S. Zhu, K. Chen, J. Huang, Development of superelastic SMA angles as seismic-resistant self-centering devices, Eng. Struct. 218 (2020) 110836.
[61] M.A. Chowdhury, A. Rahmzadeh, M.S. Alam, Improving the seismic performance of post-tensioned self-centering connections using SMA angles or end plates with SMA bolts, Smart Mater. Struct. 28 (2019) 075044.
[62] Z.-P. Chen, S. Zhu, H. Yu, B. Wang, Development of novel SMA-based D-type self-centering eccentrically braced frames, Eng. Struct. 260 (2022) 114228.
[63] B. Wang, S. Zhu, Superelastic SMA U-shaped dampers with self-centering functions, Smart Mater. Struct. 27 (2018) 055003.
[64] B. Wang, S. Zhu, F. Casciati, K. Chen, H. Jiang, Cyclic behavior and deformation mechanism of superelastic SMA U-shaped dampers under in-plane and out-of-plane loadings, Smart Mater. Struct. 30 (2021) 055009.
[65] B. Wang, S. Zhu, F. Casciati, Experimental study of novel self-centering seismic base isolators incorporating superelastic shape memory alloys, J. Struct. Eng. 146 (2020) 04020129.
[66] C. Fang, M.C. Yam, T.-M. Chan, W. Wang, X. Yang, X. Lin, A study of hybrid self-centring connections equipped with shape memory alloy washers and bolts, Eng. Struct. 164 (2018) 155–168.
[67] C. Fang, X. Zhou, A.I. Osofero, Z. Shu, M. Corradi, Superelastic SMA Belleville washers for seismic resisting applications: experimental study and modelling strategy, Smart Mater. Struct. 25 (2016) 105013.
[68] W. Wang, C. Fang, X. Yang, Y. Chen, J. Ricles, R. Sause, Innovative use of a shape memory alloy ring spring system for self-centering connections, Eng. Struct. 153 (2017) 503–515.
[69] C. Fang, W. Wang, A. Zhang, R. Sause, J. Ricles, Y. Chen, Behavior and design of self-centering energy dissipative devices equipped with superelastic SMA ring springs, J. Struct. Eng. 145 (2019) 04019109.
[70] C. Fang, W. Wang, J. Ricles, X. Yang, Q. Zhong, R. Sause, et al., Application of an innovative SMA ring spring system for self-centering steel frames subject to seismic conditions, J. Struct. Eng. 144 (2018) 04018114.
[71] N. Gao, J.-S. Jeon, D.E. Hodgson, R. DesRoches, An innovative seismic bracing system based on a superelastic shape memory alloy ring, Smart Mater. Struct. 25 (2016) 055030.
[72] E. Choi, H.D. Nguyen, J.-S. Jeon, J.-W. Kang, Self-centering and damping devices using SMA dual rings, Smart Mater. Struct. 28 (2019) 085005.
[73] C. Fang, C. Qiu, W. Wang, M.S. Alam, Self-centering structures against earthquakes: a critical review, J. Earthq. Eng. (2023) 1–36.
[74] Y. Koetaka, P. Chusilp, Z. Zhang, M. Ando, K. Suita, K. Inoue, et al., Mechanical property of beam-to-column moment connection with hysteretic dampers for column weak axis, Eng. Struct. 27 (2005) 109–117.
[75] CENTER M-AEM. Interim testing protocols for determining the seismic performance characteristics of structural and nonstructural components. 2007.
[76] MIIT, Method of constant temperature tensile test for nickel–titanium shape memory alloy wires. No. YS/T 969-2014, Ministry of Industry and Information Technology of People's Republic of China,, 2014.
[77] S. Hu, T. Guo, Y. Koetaka, Z.-P. Chen, B. Wang, M.S. Alam, et al., Seismic performance of hybrid self-centering braces with structural and nonstructural damage control functions: validation tests, computational modeling, and benefits evaluation, J. Struct. Eng. 151 (2025) 04025163.
[78] G. Abaqus, Abaqus 6.11., Dassault Systemes Simulia Corporation,, Providence, RI, USA, 2011, p. 3.